

Protrusive fingerlets drive the amphiphile-mediated disintegration of water nanodroplets in oil

Nitesh Kumar* 

Department of Chemistry, Washington State University, Pullman, WA, United States, 99163

**E-mail: nitesh.kumar@wsu.edu, kmnitesh05@gmail.com*

(Dated: April 23, 2025)

Abstract Controlling the stability and disintegration of water nanodroplets dispersed in oil is key for advancing technologies in food emulsions, pharmaceutical formulations, targeted drug delivery, and liquid-liquid separation processes. Amphiphiles self-assemble around water-in-oil nanodroplets, increasing interfacial heterogeneity, reducing droplet size, and stabilizing the emulsion systems. We present extensive all-atom molecular dynamics simulations investigating how amphiphiles modulate the heterogeneity and drive the disintegration of water nanodroplets. Utilizing network theory-based sub-ensemble analysis and curvature based geometric analysis, we characterize the amphiphile self-assembly process and the disintegration of water nanodroplets into smaller daughter droplets. We detail the microscopic mechanism of water transport from the water droplet to the oil phase, facilitated by the formation of sharp, finger-like protrusions on the droplet surface. Moreover, our results demonstrate a direct correlation between the rate of droplet disintegration and temperature-induced thermal fluctuations.

Keywords: Emulsions, Self-assembly, Protrusions, Water Nanodroplets, Surface Heterogeneity, Network theory, Molecular Dynamics Simulations, Solvent Extraction, Chemical Separations.

I. INTRODUCTION

Water-in-oil emulsions are inherently unstable and tend to separate into water and oil over time. Amphiphiles stabilize these emulsions by forming micelles around water droplets, increasing surface heterogeneity, and breaking the droplets into smaller clusters.[1–3] Although the effects of amphiphiles on emulsions are well studied, the microscopic details of how amphiphiles perturb the interfacial water structure of nanodroplets and transform them into smaller daughter droplets remain poorly understood.[4, 5] These mechanisms are fundamental in a variety of systems, ranging from colloids to liquid/liquid extraction (LLE) of energy relevant materials. Moreover, these liquid/liquid systems play a critical role in diverse fields including chemical separations, oil recovery, pharmaceuticals, and food chemistry. Understanding the structure and dynamics of water in the confinements of the nanodroplets is necessary to improve emulsion properties and controlled separations.[6–8] At elevated concentrations, amphiphiles adsorb at the nanodroplet surface and lead to the fragmentation of droplets into smaller clusters.[9] This modulation of droplet behavior is due to amphiphile effects on surface heterogeneity and the reduction of surface tension.[10]

For example, Smit et al. performed simulations to find oscillating water density on the adsorption of mi-

celle on the water/oil interface causing a spontaneous formation of surfactant monolayer, and was related to an unexpected increase in the neutron reflectivity above critical micelle concentration.[11–13] However, the perturbations in the interfacial water structure and the formation of water protrusions have not been explored. Recently, it has been shown that increasing the concentration of amphiphiles at the water/air interface leads to enhanced surface fluctuations and increased surface curvature. The presence of air, rather than oil, does not facilitate water transport and suppresses the formation of protrusion-type structures, which are considered in this study. It is also demonstrated that the surfactants at the water/oil interface enhance heterogeneity within the interfacial water structure and drive water transport into organic solvents through the surfactant-water dimer.[14] A similar mechanism was observed for the transport of ion pairs into the oil phase.[15] In this study, we aim to understand whether a similar mechanism might be relevant for the amphiphile driven transport of water from the water nanodroplet, driving the formation of daughter droplets.[16]

Enhanced surface heterogeneity enables amphiphiles to break nanodroplets into tiny water clusters of various shapes and sizes.[17, 18] Importantly, the water droplets in water-in-oil emulsions range from nanometers to micrometers. For larger droplets, amphiphile self-assembly

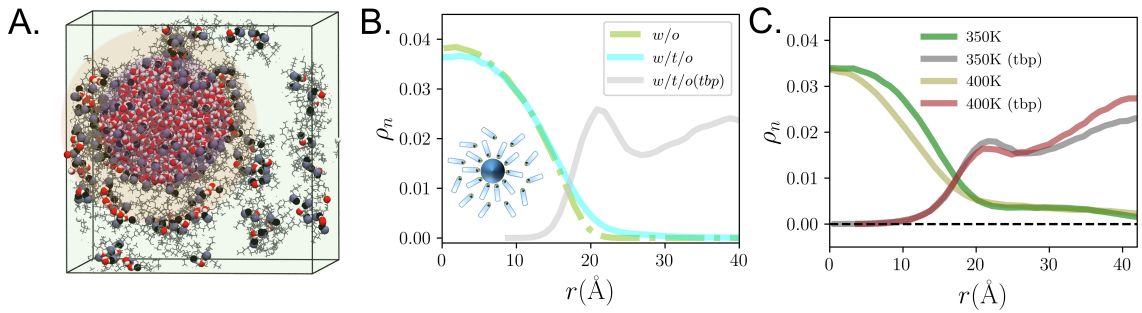


FIG. 1: (A.) A schematic illustration of the water/*tbp*/oil (w/t/o) system after 10 ns of molecular dynamics simulations at 298 K. Hexane molecules are hidden for visual clarity. (B.) Number density ($n/\text{\AA}^3$) distributions of water (cyan) and *tbp* (O=P) (grey) relative to the droplet COM present in the w/t/o system at 298 K. The density of water present in the water/oil (w/o) system is plotted in green. (C.) The number density of water and *tbp* at elevated temperatures (350 and 400 K).

and droplet disintegration can take tens of seconds, while for nanometer-sized droplets, these processes occur much faster and can be simulated computationally.[19–22] Additionally, enhancing thermal fluctuations through heating can further accelerate the amphiphile-assisted droplet disintegration process. Therefore, in this work, we explored the microscopic mechanisms of amphiphile-induced disintegration of water-in-oil nanodroplet under different temperature conditions, with a primary focus on amphiphile self-assembly, its effects on nanodroplet curvature and surface area, surface heterogeneity, and the transport mechanism of water between the nanodroplet and oil phase.

II. METHODOLOGY

All-atom molecular dynamics simulations were conducted using GROMACS 2018.2[23] on two periodic system compositions. The first system consisted of a 20 Å radius water droplet containing 1056 water molecules, immersed in a hexane solvent composed of 4087 hexane molecules. The second system was a 20 Å radius water droplet (1056 water molecules) surrounded by a mixture of *tbp* (450 molecules) and hexane (1854 molecules). The concentration of *tbp* was chosen to replicate PUREX-type conditions (with $\sim 35.94\%$ TBP by volume added to the organic phase), ensuring sufficient *tbp* to observe both self-assembly and water protrusions. The concentration has been previously characterized to transport water and ion-pairs through the formation of protrusions characterizable through simulations.[15] A lower concentration creates an ideal interface without protrusions, while an excessively high *tbp* concentration can lead to droplet

disintegration through large water clusters and potentially result in the formation of a third phase. The water/hexane system was first equilibrated for 5 ns before introducing *tbp* molecules. The temperature variation over time for both the w/o and w/t/o systems is shown in Figure S1. All systems were modeled with periodic boundary conditions to ensure the proper representation of bulk behavior. The simulations were run at three different temperatures: 298 K, 350 K, and 400 K, using the leapfrog algorithm with a 2 fs time step. The temperatures were selected to facilitate the protrusion-driven water transport mechanism. At low temperatures, this mechanism becomes sluggish, while at very high temperatures, it is significantly accelerated. Furthermore, temperatures above 400 K lead to water evaporation and potential degradation of amphiphiles such as *tbp*. Therefore, the chosen temperatures fall within a range suitable for industrial physico-chemical working conditions. Each system underwent initial energy minimization with the steepest descent algorithm, followed by 500 ps of equilibration in the NPT ensemble. The lengths of the w/o and w/t/o cubic cells after NPT simulations were 9.8 nm and 8.6 nm, respectively. Production runs were carried out in the NVT ensemble for at least 10 ns. The *tbp* and hexane were modeled using the optimized General Amber Force Field (GAFF),[14, 24] optimized to reproduce the experimental concentration of extracted water in the organic phase under standard temperature conditions,[25, 26] while water was modeled with the widely adapted TIP3P model.[27, 28] This combination of the force field is utilized to successfully characterize the water and ion-pair transport mechanisms in w/t/o systems.[14, 15] Further details are provided in ref. 15.

Short-range nonbonded electrostatic and Lennard-Jones (LJ) interactions were calculated with a 12Å cutoff. LJ cross terms were obtained using Lorentz-Berthelot combination rules. Long-range interactions were treated with the Particle Mesh Ewald (PME) method.

Network Analysis. Water networks were construed using distance based geometric criteria, specifically, the inter-oxygen atomic distance denoted as $r_{\text{cut}} < 3.5 \text{ \AA}$. [29] Utilizing this criterion, the water network adjacency matrix, \mathbf{A} , is formulated as:

$$\mathbf{A}_{ij} = \begin{cases} 1, & \text{if } r_{ij} < r_{\text{cut}}, \\ 0, & \text{otherwise.} \end{cases} \quad (1)$$

The adjacency matrix subsequently facilitates a comprehensive cluster and coordination interaction assessment. [30, 31] Within this framework, i and j signify water oxygen atoms. The principal water cluster included the intact water molecules encapsulated within the nanodroplet. The dangling water molecule were separated from the core nanodroplet using the cluster analysis module, named *connected – components*, within the NetworkX package. [32, 33] The vertices belonging to the largest connected component of water (bulk water) were separated from the remaining isolated or dangling water molecules. Connectivity analysis was then performed on the largest extracted connected component, representing an undissociated water nanodroplet.

Surface Curvature. To study the surface curvature, we first generated the triangulated coarse-grained mesh, [34, 35] derived from atomic coordinates of the w/o interfacial molecules of the largest water cluster using the pytim package. [36, 37] Subsequently, the connectivity information is used to compute surface curvature metrics using the PyVista package. [38] Detailed methodology is provided in ref. 39. Within the scope of this study, we used three distinct curvature descriptors, anchored in the principal curvatures κ_1 and κ_2 , the first one is the mean curvature, κ_m , which is equal to $\kappa_m = \frac{(\kappa_1 + \kappa_2)}{2}$, the second is the Gaussian curvature, denoted as κ_G , which is $\kappa_G = \kappa_1 \times \kappa_2$, and the third is the squared curvedness metric, κ_C^2 , which is obtained using $\kappa_C^2 = \kappa_1^2 + \kappa_2^2$. [39]

III. RESULTS AND DISCUSSION

Amphiphile self-assembly. The randomly immersed amphiphile (tri-butyl phosphate (*tbp*) in this case) can self-assemble around the water nanodroplet as a result of

dipole-dipole interactions between the polar headgroup and water hydrogen atoms. [40, 41] To explore the self-assembly of *tbp* amphiphiles around a water nanodroplet, we allowed the first 5 ns for *tbp* to self-assemble around the droplet surface. Subsequently, we plotted the density profiles of H₂O and *tbp* relative to the center of mass (COM) of the droplet (Figure 1) over the next 5 ns. This analysis was conducted in a system comprising a water nanodroplet in *tbp* and an oil solution (w/t/o) (Figure 1 A), compared to a system containing a pure water droplet in oil (w/o). Interestingly, in the first 10 ns, the *tbp* properly self-assembles around the water droplet to form a monolayer structure, with a hydrophilic head group facing the water droplet and a hydrophobic tail toward the oil phase, shown by the minima at 25 Å in the density profile of the head group (P=O atoms) of *tbp* (Figure 1 B, shown in grey color). A typical simulation snapshot showing the adsorption of *tbp* in the water droplet after 10 ns is shown in Figure 1 A. The self-assembly of *tbp* on non-transporting ideal surfaces, along with its impact on surface heterogeneity and fluctuations, has been extensively studied in previous research. [14, 25, 39, 42] In our current non-ideal and transporting systems, the H₂O density profiles show a shift in the H₂O density from the COM of the droplet to the surface of the droplet in the w/t/o system and relative droplet in the w/o system. The increased density at $r > 15 \text{ \AA}$ in the w/t/o system arises from protrusions formed on the water-in-oil nanodroplet surface in the presence of *tbp*. (*vide infra*) The thermal fluctuations due to increased temperature further deform the nanodroplet causing an increase in the density of extracted water ($r > 20 \text{ \AA}$) relative to the density at 298 K (Figure 1 C). The transport of water from the nanodroplet into the oil phase altered the self-assembly of *tbp*, as indicated by a decrease in the density of *tbp* molecules at the water-oil interface.

Nanodroplet morphology. The morphology of the intrinsic droplet surface water molecules is characterized by computing the surface curvature and areas, using the protocol described in the methodology section. The curvature and area calculations were carried out on the largest water cluster, formed primarily by the intact water molecules. Three distinct surface curvature descriptors namely, mean curvature, Gaussian curvature, and squared curvedness of the droplet were calculated. [43, 44] Figure 2 shows the distributions of instantaneous mean and Gaussian curvature of water droplet surface points at the time interval of $t = 10 \text{ ns}$. The positive and negative

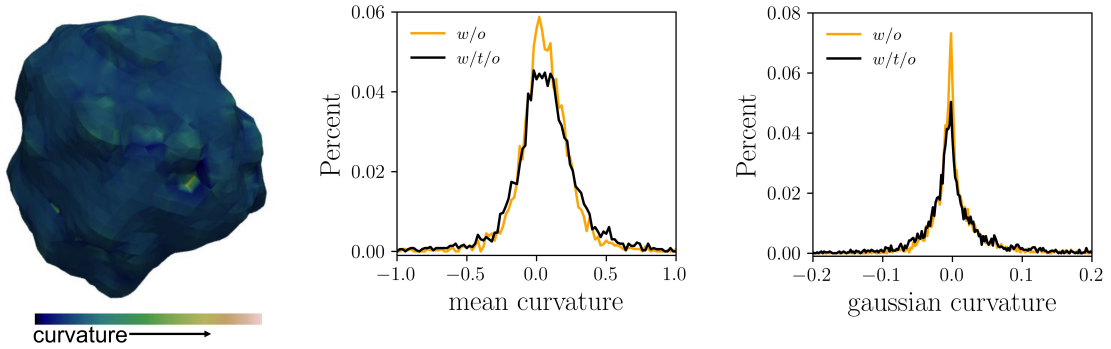


FIG. 2: Instantaneous (left panel), mean (center panel), and Gaussian (right panel) curvature distribution of the local points on the triangulated water droplet surface in w/o and w/t/o systems after 10 ns of molecular dynamics simulations at 298 K temperature. The curvature analysis is performed on the surface of the largest water cluster (as shown in the illustration) which is separated from the extracted and dangling surface water molecules using the cluster analysis as described in the Material and Methods section.

values show the convex and concave facets of the surface, respectively. A mean curvature value of zero indicates balanced curvatures at a surface point. A Gaussian curvature nearing zero can be predominantly attributed to either κ_1 or κ_2 being zero at a specific local point on the droplet surface. The range of mean and Gaussian curvatures, from positive to negative, reflects a noticeable deformation of the nanodroplet surface, primarily due to the formation of surface protrusions driven by the self-assembled *tbp* on the surface of the nanodroplet. The distributions of the average mean and Gaussian curvatures of droplet surfaces collected over the 10 ns trajectory for the w/o and w/t/o systems are provided in Figure S2 A and B respectively. For a perfect sphere with radius $r = 20 \text{ \AA}$, the anticipated average Gaussian curvature, $\frac{1}{r^2}$, is projected to be 0.0025 \AA^{-2} . The droplet significantly deviates from an ideal spherical shape, as evidenced by the broad distributions of mean and Gaussian curvatures, further enhanced by the formation of surface protrusions. The distribution becomes even broader with the addition of the *tbp* to the droplet surface, which promotes surface heterogeneity and leads to an increase in surface roughness and therefore a higher value of the surface curvatures. The two principle curvatures, κ_1 and κ_2 , can exhibit both positive and negative values depending on the local curvatures at a given point on the droplet surface. Therefore, the mean of these values (as in the mean curvature) may not comprehensively represent the intrinsic curvature behavior in numerous instances. To this end, we employed a descriptor namely, squared curvedness, which is $\kappa_1^2 + \kappa_2^2$, which intrinsically

possesses a positive value. This provides a relative depiction of the nanodroplet surface curvature within a w/t/o nanodroplet, as compared to the pure w/o system. The interplay between *tbp* and the water droplet prompts an increase in the cumulative surface curvedness of the droplet. Notably, the presence of the amphiphile *tbp* enhanced the surface curvedness by $\sim 1.57 \times$ compared to a pure water droplet within 10 ns (Figure 3 A).

The impact of amphiphile on the surface morphology is further assessed by the distribution of the area of coarse-grained water droplets in the absence and presence of the amphiphile (Figure 3B), with the distributions based on droplet area values obtained during the first 5 ns of the simulation, providing insight into the range of area changes during the initial self-assembly of TBP molecules, prior to significant droplet disintegration. The addition of amphiphiles increases the surface area of the water droplet (as shown by the broader distribution of the surface area and shift in the distribution maxima to a higher value), is primarily due to the formation of protruding water structures.[18, 39, 45] This occurs because amphiphiles, disrupt the smooth spherical shape of the droplet. The hydrophilic heads interact with water molecules, while the hydrophobic tails avoid water, leading to the formation of micelle-like structures or partial solubilization at the water-oil interface. This behavior reduces surface tension and allows the development of complex surface structures, such as water fingers or buds. The protruding water structures indicate a significant alteration in the interfacial properties of the droplet, highlighting the complex interplay between am-

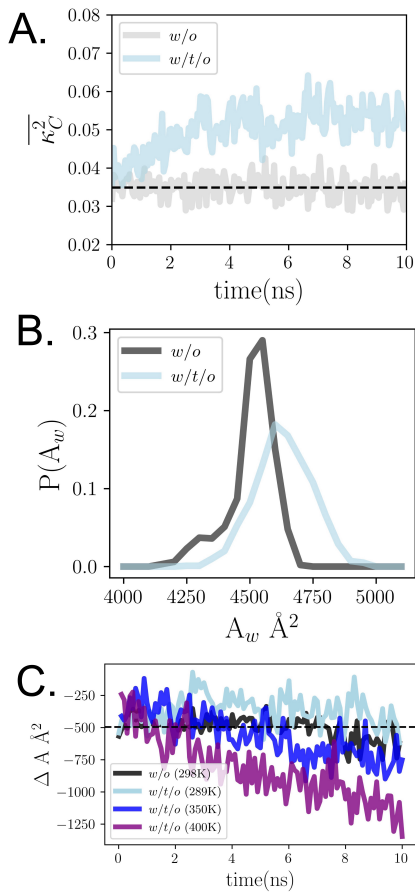


FIG. 3: (A.) The time evolution of the squared surface curvedness of the water droplet in w/o and w/t/o system. The curvature analysis is performed on the largest water cluster obtained using the water H-bonding connectivity network. (B.) The probability distribution of the nanodroplet surface area (computed for the first 5 ns) in the absence and presence of amphiphiles. (C.) The time evolution of the nanodroplet surface area at different temperatures within the w/t/o system. The change in surface area ΔA of the droplet is computed by subtracting the area of the sphere $4\pi r^2$ from the area of the triangulated droplet surface, obtained from the largest intact water cluster, excluding the transported and the dangling water molecules. The transport of water to the oil phase gradually reduces the number of water molecules in the droplet, making the resulting structure to become smaller than an ideal sphere of radius r .

phiphiles and water molecules. We then characterized how the increase in thermal fluctuations impacts the surface morphology by quantifying the surface area of water droplets at three different temperatures (298, 350, and 400 K) in the presence of tbp as a function of time, as illustrated in Figure 3 C. The surface area of a pure spherical droplet with a radius of 20 \AA , calculated using

the formula $A = 4\pi r^2$, was subtracted from the surface area of the intact triangulated droplet surface, excluding the dangling and extracted water molecules. At elevated temperatures, the self-assembled amphiphiles not only increase the roughness of the droplet surface by forming protruding structures, but also accelerate the droplet disintegration rate (*vide infra*). As a result, the droplets start to break into smaller clusters at a much faster rate compared to normal temperature conditions. This is also observed in the faster decay of ΔA , as shown in Figure 3. In this figure, the negative values of ΔA indicate that the triangulated mesh droplets have a surface area slightly smaller than that of a perfect sphere, due to shape heterogeneity caused by water dynamics and the amphiphiles on the surface. The deformation induced by tbp resulted in an increase in the droplet surface area compared to a droplet in oil without tbp . The increase in system temperature further amplified shape heterogeneity and water transport, as evidenced by the reduction in nanodroplet surface area, and decrease in the overall size of the droplet over time. This change in surface area is related to dynamic protruding water structures and in turn possibly related to the experimentally observed enhanced reactivity on the water surfaces.[46–50]

Nanodroplet heterogeneity. Upon the addition of amphiphile, there was an increase in the heterogeneity of the droplet water structure, leading to more extracted and surface-dangling water molecules. To understand the evolution of perturbations in the water structure of a water droplet induced by surface-assembled tbp , we conducted a comprehensive cluster analysis of the network of water. This analysis allowed us to compare the water network in the presence of tbp to that in a pure system without tbp . The evolution of the number of water clusters with time is shown in Figure 4 A. The total number of water clusters, N_C , remained below 20 throughout the simulation, with an average value of about 16. Adding tbp to the oil phase caused the water droplet to disintegrate, increasing the number of water clusters from $N_C = 20$ at $t = 0$ to $N_C = 80$ at $t = 10$ ns. Visual representations of the simulation, showing the water droplet at $t = 0, 10,$ and 60 ns, are provided in Figure S3. Increasing the temperature accentuated the heterogeneity of the nanodroplet, raising the total cluster count to 150 at 350 K (Figure S4). A further temperature increase raised the N_C value to about 230 at 400 K. This rise in water clusters at higher temperatures is mainly due to the enhanced disintegration dynamics of the nan-

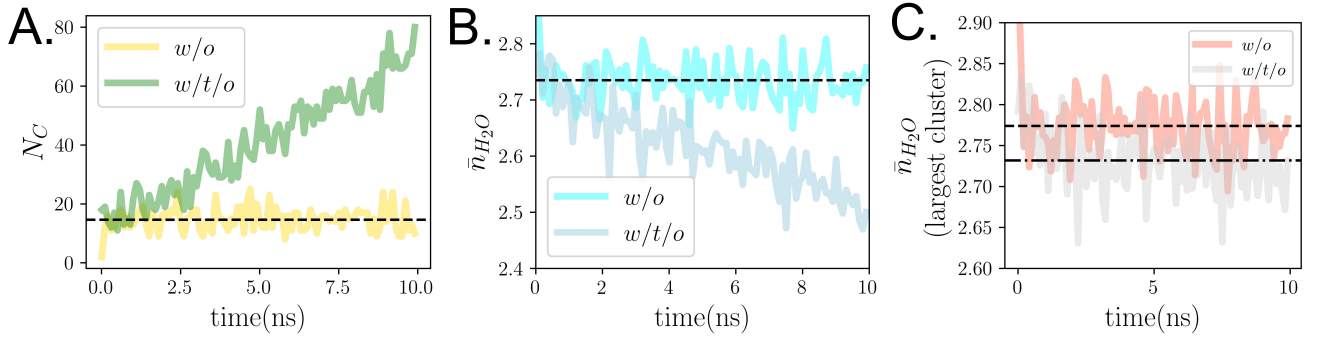


FIG. 4: Time evolution of the (A) number of water clusters (N_C), (B) average H_2O coordination (\bar{n}_{H_2O}) number and (C) the largest water-cluster coordination number (\bar{n}_{max,H_2O}) in the w/o and w/t/o systems at 298 K temperature. The mean values are represented by the dashed black lines.

odroplet. Detailed analyses of droplet topologies were conducted based on the average water connectivity (Ow coordination), as shown in Figure 4. In the intrinsic environment of the water-in-oil droplet, water interacted with nearly 2.73 adjacent water molecules. However, the introduction of *tbp* caused the water droplet to disintegrate, reducing water connectivity to $\bar{n}_{H_2O} = 2.5$ within the first 10 ns of the simulation. The increase in temperature further decreased $\bar{n}_{H_2O} = 2.15$ at 350K to ~ 1.85 at 400 K (Figure S4). Comprehensive calculations of the average H_2O coordination, associated with the most predominant water cluster (excluding extracted and dangling water molecules via cluster analysis), are shown in Figure 4 C. The coordination of the largest water cluster (\bar{n}_{max,H_2O}) evolved constantly over time. Similar trends are obtained at different temperatures (Figure S4 C). The results suggest that the time decay of disruptions within the water network (in terms of the average water coordination number) in the w/t/o system primarily arises from the dangling and extracted water molecules, while the coordination of the intact core nanodroplet remains constant, fluctuating around a stable water coordination number. Nonetheless, this average coordination number of the intact core nanodroplet (\bar{n}_{max,H_2O}) decreased both in the presence of amphiphile (Figure 4 C) and due to the action of temperature (Figure S4), due to increased heterogeneity within the hydrogen bonding network of water.

Protrusion driven water transport. Based on our theoretical framework, we postulated that the perturbations within the water network predominantly stem from the dangling water entities engaged in surface protrusions, thereby facilitating the transport of water from

the droplet to the oil phase.[45, 51] To support this hypothesis, we presented the two-dimensional spatial density $\rho(x, y)$ distribution of the water droplet, in the systems with and without *tbp*, as shown in Figure 5. The distributions show that the interaction between *tbp* and the water droplet creates significant interfacial heterogeneity leading to the formation of water microchannels and protrusions of different shapes and sizes near the droplet surface. These surface-structures were responsible for driving water transport from the droplet surface to the oil phase.[14, 15] Protrusion-driven water transport can be envisioned as a unidirectional transport mechanism, distinct from other mechanisms such as diffusion. This is because it is highly unlikely for water disintegrating via protrusion formation to follow the exact same pathway back to the larger droplet. The increased number of pathways makes protrusion-driven water transport unique, warranting further studies to fully uncover its thermodynamics and kinetics under various conditions. A typical simulation snapshot showing the transport of water through the protruding structure is depicted in Figure 5 C. Some differences in the structure of protrusions can be expected based on factors such as amphiphile concentration, topology (including chain length or polar groups), and other physico-chemical conditions. Importantly, these protruding surface structures create tailored microenvironments that enhance chemical reactivity and catalysis, providing a favorable environment for liquid/liquid surface reactions.[52]

Kinetics of water transport. We analyzed the kinetics of water transfer from the droplet boundary to the oil phase using the droplet disintegration rates. In our system with constant parameters—total water molecule

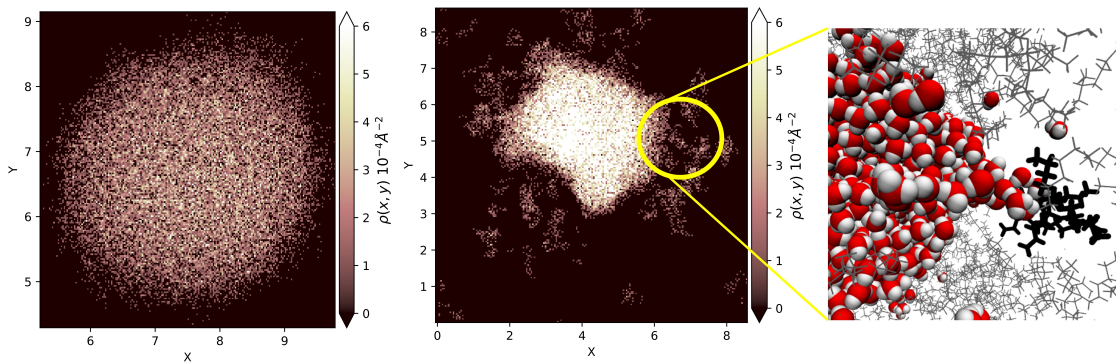


FIG. 5: Two dimensional density distribution $\rho(x, y)$ of water droplet present in w/o (left panel) and w/t/o (center panel) systems. The right panel shows a representative snapshot of water extraction by *tbp* (shown in black) through protrusions. Note that the density distributions are averaged over 100 ps after the 10 ns evolution of the molecular dynamics trajectory.

count (n_w), volume, and temperature—the water in the oil (n_{oil}) and droplet (n_d) phases is conserved, i.e., $n_{oil} + n_d = n_w$. Assuming that the disintegration of the nanodroplet follows the first-order kinetics, i.e., $\frac{dn_d}{dt} \propto -n_d$. Solving this equation gives,

$$n_d(t) = n_{d,0}e^{-t/\tau}, \quad (2)$$

where $n_{d,0}$ is the initial number of water molecules in the nanodroplet, and τ is the droplet disintegration lifetime. Herein, the conservation law implies that the rate of water transfer to the oil phase is given by, $\frac{dn_{oil}}{dt} \propto -\frac{dn_d}{dt} \propto n_d$. Integrating, the number of water molecules in the oil phase evolves as, $n_{oil}(t) = n_{oil,0} + n_{d,0}(1 - e^{-t/\tau})$, where $n_{oil,0}$ is the number of water in the oil phase at the initial time. Notably, for this calculation, dangling water molecules at the droplet interface are considered to have moved to the oil phase. This formulation points that as $t \rightarrow \infty$, $n_d \rightarrow 0$ and $n_{oil} \rightarrow n_w$, indicating the complete disintegration of the nanodroplet at infinite time. However, the state of complete nanodroplet disintegration is challenging to achieve through unconstrained all-atom classical simulations. Therefore, we focused on fitting only the initial decay phase of water loss from the nanodroplet. Our initial efforts were directed towards fitting the n_d values of the droplets against time t (in nanoseconds) at temperatures 298 K and 350 K. This was achieved using a linear regression model, and a first-order decay function in alignment with Equation 2 (Figure S5).[53] However, at an elevated temperature of 350 K, deviations from both linear and first-order decay mechanisms were observed after 10 ns. This suggests that the decay mechanism follows a more complex pathway.[54, 55] To comprehensively understand the nan-

droplet disintegration process, we used a stretched exponential formulation, which typically describes complex relaxation processes,

$$n_d(t) = n_{d,0}e^{\left(-\frac{t}{t_0}\right)^\beta} \quad (3)$$

here, t_0 denotes the characteristic relaxation time, related to the time taken by the droplet to reach equilibrium after being disturbed by the adsorbed amphiphiles. The factor β is the exponent of the stretched exponential,[56] and $n_{d,0}$ is the initial number of H₂O in the droplet. The respective values of t_0 and β are provided in Figure S6.

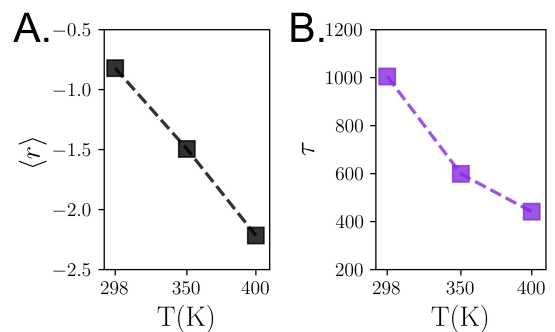


FIG. 6: (A) The average droplet disintegration rate ($\langle r \rangle$) ([H₂O/ns]) and (B) droplet lifetime (in ns) as a function of system temperature. The droplet disintegration rate became faster and the average droplet lifetime decreased with an increase in temperature.

From these kinetic analysis, we observe that the disintegration of the droplet becomes faster and the respective rates r , obtained using the formula $(n(t + \Delta t) - n(t))/\Delta t$, where $n(t)$ and $n(t + \Delta t)$ are the number of water in the

intact nanodroplet at time t and $t + \Delta t$, respectively, increase linearly with temperature, from -0.82 [H₂O]/ns at 298 K to -2.21 [H₂O]/ns at 400 K (Figure 6 A). The stretched exponent β decreased linearly from ~ 1.25 at 298 K to ~ 0.12 at 400 K. The characteristic relaxation times t_0 of the water nanodroplet increase with temperature, mainly due to the increase in instantaneous rates of droplet disintegration and formation relative to the droplet at 298 K. The average lifetime of the droplet, τ , obtained using equation 2 decreases from ~ 1004.73 ns at 298 K to ~ 441.2 ns at 400 K (Figure 6 B), clearly demonstrating the effect of temperature on droplet disintegration, with higher temperatures leading to significantly shorter nanodroplet disintegration times. In future studies, we will investigate whether the relaxation of water nanodroplets under various physicochemical conditions follows a stretched exponential trend and assess the universality of this relaxation behavior, and in turn the universality of protrusion-driven disintegration mechanics of nano- to micro-sized droplets.

IV. CONCLUSIONS

In this study, we have presented the microscopic behavior of water-in-oil nanodroplet and its disintegration in the presence of *tbp* amphiphiles. Our findings reveal that *tbp* molecules adsorb at the water droplet surface, forming a layered structure, which increases the surface area and curvature compared to pure nanodroplets without amphiphile. The adsorbed *tbp* enhances the surface heterogeneity of the nanodroplet, disrupting the water structure and leading to the disintegration of the nanodroplet into smaller water clusters, a process that accelerates linearly with increasing temperature. We also observed that interfacial *tbp* facilitates the transport of interfacial water to the organic phase by forming surface-specific morphological features known as protrusions. These finger-like protrusions resemble the morphologies observed in solvent extraction systems that mediate the transport of ion pairs from the aqueous to the oil phase. The insights provided in this study are fundamental in understanding the microscopic behavior of water-in-oil nanodroplets in emulsions, and the mechanisms of liquid/liquid extraction in the presence of amphiphiles for controlled chemical separation.

Acknowledgments

NK thanks the Center for Institutional Research Computing (CIRC) at Washington State University for computational resources. NK thanks PNNL-WSU DGRP for financial support.

Conflicts of Interest

None.

Supplementary Information

Mean and Gaussian Curvature, Simulation Snapshots, Water Cluster, Fitting Functions, Relaxation times.

Data Availability

The datasets generated during this study, along with details of the algorithms used, are provided in the main text and Supplementary Information. Molecular dynamics simulation input files are available from the corresponding author upon reasonable request.

References

- [1] Shi, C.; Zhang, L.; Xie, L.; Lu, X.; Liu, Q.; He, J.; Mantilla, C. A.; Van den Berg, F. G.; Zeng, H. Surface interaction of water-in-oil emulsion droplets with interfacially active asphaltenes. *Langmuir* **2017**, *33*, 1265–1274.
- [2] Xu, F.; Fang, Z.; Yang, D.; Gao, Y.; Li, H.; Chen, D. Water in oil emulsion stabilized by tadpole-like single chain polymer nanoparticles and its application in biphasic reaction. *ACS applied materials & interfaces* **2014**, *6*, 6717–6723.
- [3] Kilpatrick, P. K. Water-in-crude oil emulsion stabilization: review and unanswered questions. *Energy & Fuels* **2012**, *26*, 4017–4026.
- [4] Tcholakova, S.; Vankova, N.; Denkov, N. D.; Danner, T. Emulsification in turbulent flow:: 3. Daughter drop-size distribution. *Journal of Colloid and Interface Science* **2007**, *310*, 570–589.
- [5] Sun, X.; Zeng, H.; Tang, T. Molecular simulations on the coalescence of water-in-oil emulsion droplets with non-ionic surfactant and model asphaltene. *Langmuir* **2023**, *39*, 2233–2245.
- [6] Gradzielski, M.; Duvail, M.; de Molina, P. M.; Simon, M.; Talmon, Y.; Zemb, T. Using microemulsions: formula-

- tion based on knowledge of their mesostructure. *Chemical reviews* **2021**, *121*, 5671–5740.
- [7] Levinger, N. E. Water in confinement. *Science* **2002**, *298*, 1722–1723.
- [8] Sofronov, O. O.; Bakker, H. J. Slow proton transfer in nanoconfined water. *ACS central science* **2020**, *6*, 1150–1158.
- [9] Li, N.; Sun, Z.; Pang, Y.; Qi, Z.; Liu, W.; Li, W.; Sun, M.; Li, B.; Wang, Z. Microscopic mechanism for electrocoalescence of water droplets in water-in-oil emulsions containing surfactant: A molecular dynamics study. *Separation and Purification Technology* **2022**, 120756.
- [10] Phan, C. M. Affinity of Amphiphilic Molecules to Air/Water Surface. *ACS omega* **2023**, *8*, 47928–47937.
- [11] Smit, B.; Hilbers, P.; Esselink, K.; Rupert, L.; Van Os, N.; Schlijper, A. Computer simulations of a water/oil interface in the presence of micelles. *Nature* **1990**, *348*, 624–625.
- [12] Kurokawa, T.; Urakami, N.; Yaegashi, K. N.; Sakashita, A.; Imai, M.; Yamamoto, T. Molecular dynamics simulation for morphological change of water-in-oil microemulsion droplets induced by addition of polymer chains. *Soft Matter* **2011**, *7*, 7504–7510.
- [13] Jian, C.; Liu, Q.; Zeng, H.; Tang, T. Effect of model polycyclic aromatic compounds on the coalescence of water-in-oil emulsion droplets. *The Journal of Physical Chemistry C* **2017**, *121*, 10382–10391.
- [14] Servis, M. J.; Clark, A. E. Surfactant-enhanced heterogeneity of the aqueous interface drives water extraction into organic solvents. *Physical Chemistry Chemical Physics* **2019**, *21*, 2866–2874.
- [15] Kumar, N.; Clark, A. E. Unexpected inverse correlations and cooperativity in ion-pair phase transfer. *Chemical science* **2021**, *12*, 13930–13939.
- [16] Sicard, F.; Toro-Mendoza, J.; Striolo, A. Nanoparticles actively fragment armored droplets. *ACS nano* **2019**, *13*, 9498–9503.
- [17] Znamenskiy, V.; Marginean, I.; Vertes, A. Solvated ion evaporation from charged water nanodroplets. *The Journal of Physical Chemistry A* **2003**, *107*, 7406–7412.
- [18] Ichiki, K.; Consta, S. Disintegration mechanisms of charged aqueous nanodroplets studied by simulations and analytical models. *The Journal of Physical Chemistry B* **2006**, *110*, 19168–19175.
- [19] Wang, B.-B.; Wang, X.-D.; Yan, W.-M.; Wang, T.-H. Molecular dynamics simulations on coalescence and non-coalescence of conducting droplets. *Langmuir* **2015**, *31*, 7457–7462.
- [20] Li, S.; Yuan, S.; Zhang, Y.; Guo, H.; Liu, S.; Wang, D.; Wang, Y. Molecular dynamics study on the demulsification mechanism of water-in-oil emulsion with SDS surfactant under a DC electric field. *Langmuir* **2022**, *38*, 12717–12730.
- [21] Paliy, M.; Consta, S.; Yang, J. Interactions between carbon nanoparticles in a droplet of organic solvent. *The Journal of Physical Chemistry C* **2014**, *118*, 16074–16086.
- [22] Li, N.; Pang, Y.; Sun, Z.; Sun, X.; Li, W.; Sun, Y.; Zhu, L.; Li, B.; Wang, Z.; Zeng, H. Unraveling Partial Coalescence Between Droplet and Oil–Water Interface in Water-in-Oil Emulsions under a Direct-Current Electric Field via Molecular Dynamics Simulation. *Langmuir* **2024**, *40*, 5992–6003.
- [23] Van Der Spoel, D.; Lindahl, E.; Hess, B.; Groenhof, G.; Mark, A. E.; Berendsen, H. J. GROMACS: fast, flexible, and free. *Journal of computational chemistry* **2005**, *26*, 1701–1718.
- [24] Wang, J.; Wolf, R. M.; Caldwell, J. W.; Kollman, P. A.; Case, D. A. Development and testing of a general amber force field. *Journal of computational chemistry* **2004**, *25*, 1157–1174.
- [25] Ye, X.; Cui, S.; de Almeida, V. F.; Khomami, B. Molecular simulation of water extraction into a tri-n-butylphosphate/n-dodecane solution. *The Journal of Physical Chemistry B* **2013**, *117*, 14835–14841.
- [26] Mu, J.; Motokawa, R.; Williams, C. D.; Akutsu, K.; Nishitsuji, S.; Masters, A. J. Comparative molecular dynamics study on tri-n-butyl phosphate in organic and aqueous environments and its relevance to nuclear extraction processes. *The Journal of Physical Chemistry B* **2016**, *120*, 5183–5193.
- [27] Jorgensen, W. L.; Chandrasekhar, J.; Madura, J. D.; Impey, R. W.; Klein, M. L. Comparison of simple potential functions for simulating liquid water. *The Journal of chemical physics* **1983**, *79*, 926–935.
- [28] Mark, P.; Nilsson, L. Structure and dynamics of the TIP3P, SPC, and SPC/E water models at 298 K. *The Journal of Physical Chemistry A* **2001**, *105*, 9954–9960.
- [29] Luzar, A.; Chandler, D. Hydrogen-bond kinetics in liquid water. *Nature* **1996**, *379*, 55–57.
- [30] Ozkanlar, A.; Clark, A. E. ChemNetworks: A complex network analysis tool for chemical systems. *Journal of computational chemistry* **2014**, *35*, 495–505.
- [31] Kumar, N.; Servis, M. J.; Liu, Z.; Clark, A. E. Competitive interactions at electrolyte/octanol interfaces: a molecular perspective. *The Journal of Physical Chemistry C* **2020**, *124*, 10924–10934.
- [32] Hagberg, A.; Swart, P.; S Chult, D. *Exploring network structure, dynamics, and function using NetworkX*; 2008.
- [33] Kumar, N. Exclusive ion recognition using host-guest sandwich complexes. *Physical Chemistry Chemical Physics* **2024**, *26*, 3152–3158.
- [34] Willard, A. P.; Chandler, D. Instantaneous liquid interfaces. *The Journal of Physical Chemistry B* **2010**, *114*, 1954–1958.
- [35] Lorensen, W. E.; Cline, H. E. *Seminal graphics: pioneer-*

- ing efforts that shaped the field; 1998; pp 347–353.
- [36] Sega, M.; Fábíán, B.; Jedlovsky, P. Layer-by-layer and intrinsic analysis of molecular and thermodynamic properties across soft interfaces. *The Journal of chemical physics* **2015**, *143*, 114709.
- [37] Sega, M.; Hantal, G.; Fábíán, B.; Jedlovsky, P. Pytim: A python package for the interfacial analysis of molecular simulations. 2018.
- [38] Sullivan, C. B.; Kaszynski, A. PyVista: 3D plotting and mesh analysis through a streamlined interface for the Visualization Toolkit (VTK). *Journal of Open Source Software* **2019**, *4*, 1450.
- [39] Kumar, N.; Bilsky, J.; Clark, A. E. Isotropic anisotropic surface geometry transitions induced by adsorbed surfactants at water/vapor interfaces. *The Journal of Chemical Physics* **2024**, *161*.
- [40] Smolentsev, N.; Roke, S. Self-assembly at water nanodroplet interfaces quantified with nonlinear light scattering. *Langmuir* **2020**, *36*, 9317–9322.
- [41] Hande, V. R.; Chakrabarty, S. Exploration of the presence of bulk-like water in AOT reverse micelles and water-in-oil nanodroplets: the role of charged interfaces, confinement size and properties of water. *Physical Chemistry Chemical Physics* **2016**, *18*, 21767–21779.
- [42] Baaden, M.; Burgard, M.; Wipff, G. TBP at the water-oil interface: the effect of TBP concentration and water acidity investigated by molecular dynamics simulations. *The Journal of Physical Chemistry B* **2001**, *105*, 11131–11141.
- [43] Braun, A. R.; Sevcsik, E.; Chin, P.; Rhoades, E.; Tristram-Nagle, S.; Sachs, J. N. α -Synuclein induces both positive mean curvature and negative Gaussian curvature in membranes. *Journal of the American Chemical Society* **2012**, *134*, 2613–2620.
- [44] Koenderink, J. J.; Van Doorn, A. J. Surface shape and curvature scales. *Image and vision computing* **1992**, *10*, 557–564.
- [45] Benjamin, I. Structure, thermodynamics, and dynamics of thiocyanate ion adsorption and transfer across the water/toluene interface. *The Journal of Physical Chemistry B* **2022**, *126*, 5706–5714.
- [46] Kusaka, R.; Nihonyanagi, S.; Tahara, T. The photochemical reaction of phenol becomes ultrafast at the air–water interface. *Nature Chemistry* **2021**, *13*, 306–311.
- [47] Ishiyama, T.; Tahara, T.; Morita, A. Why the photochemical reaction of phenol becomes ultrafast at the air–water interface: The effect of surface hydration. *Journal of the American Chemical Society* **2022**, *144*, 6321–6325.
- [48] Ruiz-Lopez, M. F.; Francisco, J. S.; Martins-Costa, M. T.; Anglada, J. M. Molecular reactions at aqueous interfaces. *Nature Reviews Chemistry* **2020**, *4*, 459–475.
- [49] Chen, H.; Wang, R.; Chiba, T.; Foreman, K.; Bowen, K.; Zhang, X. Designer “Quasi-Benzyne”: The Spontaneous Reduction of Ortho-Diiodotetrafluorobenzene on Water Microdroplets. *Journal of the American Chemical Society* **2024**, *146*, 10979–10983.
- [50] Piradashvili, K.; Alexandrino, E. M.; Wurm, F. R.; Landfester, K. Reactions and polymerizations at the liquid–liquid interface. *Chemical reviews* **2016**, *116*, 2141–2169.
- [51] Koizumi, A.; Tahara, H.; Hirano, T.; Morita, A. Revealing transient shuttling mechanism of catalytic ion transport through liquid–liquid interface. *The Journal of Physical Chemistry Letters* **2020**, *11*, 1584–1588.
- [52] Ghadar, Y.; Clark, A. E. Intermolecular network analysis of the liquid and vapor interfaces of pentane and water: microsolvation does not trend with interfacial properties. *Physical Chemistry Chemical Physics* **2014**, *16*, 12475–12487.
- [53] Li, H.; Zeng, X. C. Wetting and interfacial properties of water nanodroplets in contact with graphene and monolayer boron–nitride sheets. *ACS nano* **2012**, *6*, 2401–2409.
- [54] Ruiz Pestana, L.; Head-Gordon, T. Evaporation of water nanodroplets on heated surfaces: Does nano matter? *ACS nano* **2022**, *16*, 3563–3572.
- [55] Malek, S. M.; Poole, P. H.; Saika-Voivod, I. Thermodynamic and structural anomalies of water nanodroplets. *Nature communications* **2018**, *9*, 2402.
- [56] Berberan-Santos, M.; Bodunov, E.; Valeur, B. Mathematical functions for the analysis of luminescence decays with underlying distributions 1. Kohlrausch decay function (stretched exponential). *Chemical Physics* **2005**, *315*, 171–182.